Slow approach to steady motion of a concave body in a free-molecular gas

Tetsuro Tsuji, Junichi Arai, and Satoyuki Kawano*
Graduate School of Engineering Science, Osaka University, Japan
(Received 1 June 2015; published 23 July 2015)

A body in a free-molecular gas accelerated by a constant external force is considered on the basis of kinetic theory. The body is an infinitely long rectangular hollow column with one face removed, and thus it has a squarish U-shaped cross section. The concave part of the body points toward the direction of motion, and thus the gas molecules may be trapped in the concavity. Gas molecules undergo diffuse reflection on a base part, whereas specular reflection on two lateral parts. It is numerically shown that the velocity of the body approaches a terminal velocity, for which a drag force exerted by the gas counterbalances the external force, in such a way that their difference decreases in proportion to the inverse square of time for a large time. This rate of approach is slower than the known rate proportional to the inverse cube of time in the case of a body without concavity [Aoki *et al.*, Phys. Rev. E **80**, 016309 (2009)]. Based on the detailed investigation on the velocity distribution function of gas molecules impinging on the body, it is clarified that the concavity prevents some molecules from escaping to infinity. This trapping enhances the effect of recollision between the body and the gas molecules, which is the cause of the inverse power laws, and thus leads to the slower approach.

DOI: 10.1103/PhysRevE.92.012130 PACS number(s): 05.20.Dd, 47.45.Ab, 51.10.+y, 47.11.−j

I. INTRODUCTION

Free motion of a body in a fluid has been of interest in fluid mechanics as well as in statistical mechanics. In the former case, the fluid is treated as a continuum and thus only macroscopic variables are involved. On the other hand, in the latter case, the fluid is a collection of molecules. In either treatment, when the body moves in a time-dependent manner, the history of the motion may influence the motion in the future and thus a long-time behavior. However, a time-dependent drag on the body exerted by the fluid may have different features between the two treatments. In the present paper, we are interested in the role of the history effect on the time-dependent behavior of the body, especially when we apply the latter treatment and the body has a concave part.

Before getting to the main point, let us introduce the familiar example of a motion with a history effect: the rectilinear motion of a sphere immersed in a Stokes fluid (incompressible viscous fluid without nonlinear term). Such a motion can be described by the Basset-Boussinesq-Oseen equation that contains the history integral (e.g., Refs. [1,2]; cf. Ref. [3] for a more general case with a nonuniform flow field). Suppose that a constant external force acts on the sphere. As time goes on, the velocity $\mathcal{V}$ of the sphere approaches its terminal velocity $\mathcal{V}_\infty$ for which the drag acting on the sphere counterbalances the external force. It is shown in Ref. [4] that the difference $|\mathcal{V}_\infty - \mathcal{V}|$ decreases in proportion to $t_*^{-1/2}$ for large t_* (i.e., the rate of approach is $t_*^{-1/2}$), where t_* is the time variable. In contrast, if the history effect is neglected, the rate is exponentially fast in time. In order to know the response of a body in a fluid to an external force, the correct description of the history effect may be necessary. The importance of the history effect in a viscous flow is studied numerically [5,6] or experimentally [7] (see also references therein).

When a fluid is treated as a collection of molecules, the history effect appears in a different manner. By the use of kinetic theory (e.g., Refs. [8,9]), the long-time behavior of a body immersed in a rarefied gas under an external force has been studied in the literature, both mathematically [10–17] and numerically [18–22] (see also the monograph [23]). Most of these studies are devoted to the case of a free-molecular gas, that is, the gas is so rarefied that intermolecular collisions may be neglected. Let us introduce one of the results for a free-molecular gas [10]: the rectilinear motion of a d dimensional disk in its perpendicular direction. Note that the body is an infinite plate for $d = 1$ and an infinitely long plate with a finite width for $d = 2$. Moreover, the interaction between the body and the gas molecules is assumed to be specular reflection, and the gas is set to an equilibrium at an initial time. The disk is accelerated by a constant external force and approaches the steady motion with a terminal velocity as time goes on, as in the above-mentioned example of the sphere in a Stokes fluid; however, now the rate is proportional to t_*^{-d-2} for large t_* [10]. The inverse power law with an integer exponent is attributed to a recollision, which is the collision between the body and the molecule that has already collided with the body in the past. Recollision is the history effect peculiar to a highly rarefied gas. This mathematical result is extended to the cases with the different type of an external force [11], a general convex body [12] (convex toward a gas domain), different boundary conditions [13,16,17], an elastic body [14], and a body with a concave part [15]. For the physical background of these studies, the readers are referred to the monograph [23]. Some other related studies are presented as follows. The history effects on the motion of a particle weakly coupled to a dense ideal Bose gas is studied in Ref. [24], and the motion of a particle interacting with surrounding particles via short-range potential is in Ref. [25] (see also references therein).

The numerical studies are also carried out using diffuse reflection as the interaction between a body and gas molecules [18–22] in order to complement (and extend) the mathematical works [10–13] and to make the results visible things. The motivation of the numerical works is the following. First, the mathematical results are based on the assumption that the difference between an initial velocity and a terminal

*kawano@me.es.osaka-u.ac.jp

velocity is sufficiently smaller than a thermal speed at an initial equilibrium. This assumption is imposed solely by a technical issue and not by a physical situation. Second, the mathematical estimates cannot give the full solution to the present problem. Therefore, the detailed information of the solution, e.g., the velocity distribution function, is missing. Finally, the numerical works are able to treat the cases that are difficult for mathematical analysis (e.g., the case of many oscillations under an external elastic force [19], the case of a gas with a special interaction with background [20], and the case of a collisional gas [21,22]). In the present paper, we try to complement the mathematical result of a two- or three-dimentional concave body with specular reflection [15], in which the rate of approach is proved to be proportional to t_*^{-3} under the above-mentioned smallness assumption. This is slower than the rate for a convex body t_*^{-4} for $d = 2$ (or t_*^{-5} for $d = 3$) [10] and is independent of d. We apply the diffuse-reflection condition for the part of the concave body and give the corresponding numerical evidence of the slower approach, without the smallness assumption. The dependence of the rate on the degree of concavity (H in Sec. II A) is systematically investigated. Moreover, we visualize the effect of recollision at the level of a velocity distribution function in order to explain the physical origin of the slower rate. Let us close this section by noting that for diffuse reflection, the rate is t_*^{-d-1} for a convex body [13,16–18].

II. FORMULATION

A. Description of the problem

Let us consider a concave body in an infinite expanse of an ideal monatomic gas. The body is an infinitely long rectangular hollow column with one face removed, and thus it has a squarish U-shaped cross section (Fig. 1). More specifically, the concave body consists of three infinite plates: a base plate of width L and two lateral plates of width H, where the thickness δ of the plates are neglected, i.e., $\delta \to 0$. Each lateral plate

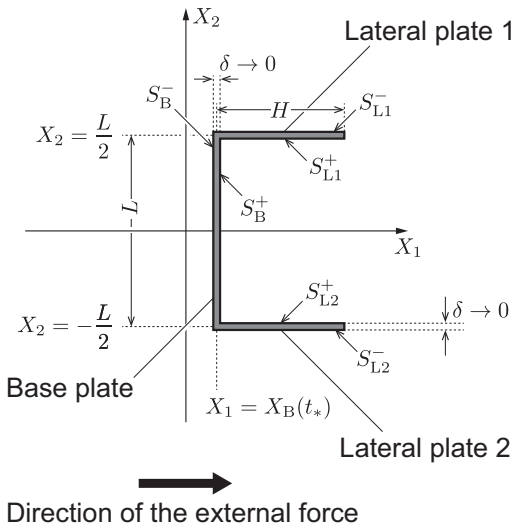

FIG. 1. A concave body considered in Ref. [15] and in the present problem. The case of $H \to 0$ corresponds to the previous studies [10,11,13,16–18,20].

is connected to, respectively, the both sides of the base plate in such a way that the angles between the lateral and the base plates are orthogonal (Fig. 1). We introduce the Cartesian coordinates $\boldsymbol{X} = (X_1, X_2, X_3)$ in space. The concavity of the body points the positive X_1 direction as described in Fig. 1. The position of the body $X_1 = X_B(t_*)$ is defined as the position of the base plate. Then we define the faces of plates as follows (Fig. 1):

$$S_B^{\pm}(t_*) = \{X_1 = X_B(t_*) \pm 0, \quad X_2 \in [-L/2, L/2], \quad X_3 \in \mathbb{R}\}, \tag{1a}$$

$$S_{L1}^{\pm}(t_*) = \{X_1 \in [X_B(t_*), X_B(t_*) + H], \quad X_2 = L/2 \mp 0, \quad X_3 \in \mathbb{R}\}, \tag{1b}$$

$$S_{L2}^{\pm}(t_*) = \{X_1 \in [X_B(t_*), X_B(t_*) + H], \quad X_2 = -L/2 \pm 0, \quad X_3 \in \mathbb{R}\}, \tag{1c}$$

where we name the lateral plates at $X_2 = L/2$ and $X_2 = -L/2$ as plate 1 and plate 2, respectively. In Eq. (1) and what follows, upper and lower signs go together. The body is subject to an external force $M_* F_*$ and a drag force G_* exerted by the surrounding gas, where M_* is the mass of the body. The drag G_* and the mass M_* are the quantities per unit length in the X_3 direction, and we will introduce the equation of motion per unit length later. The motion of the concave body is restricted to the translation in the X_1 direction, i.e., the rotation of the body and the translation in the other directions X_j ($j = 2, 3$) are not considered.

The gas and the body is in an equilibrium at an initial time $t_* = 0$. To be more specific, the gas is initially set to a uniform thermal equilibrium at rest with a density ρ_0 and a temperature T_0. Moreover, the body is kept at a uniform and constant temperature T_0. Under these settings, the body sets in motion induced by the external force at $t_* = 0$. As time proceeds, the velocity $V_B(t_*)$ of the body (in the X_1 direction) approaches a terminal velocity $V_{B\infty} \equiv \lim_{t_* \to \infty} V_B(t_*)$ so that the drag force exerted by the gas counterbalances the external force. We study the approach of V_B to $V_{B\infty}$ under the following assumptions:

(1) The gas is so rarefied that the interaction between the gas molecules are neglected. Such a gas is called a free-molecular gas (or, equivalently, a Knudsen gas) [8,9]. The behavior of the gas is described by the free transport equation of the molecular velocity distribution function, namely the Boltzmann equation without the collision term.

(2) The velocities of molecules reflected on $S_B^{\pm}$ are distributed according to a Maxwellian distribution characterized by the temperature and the velocity of the body, where the density is determined in such a way that there is no net mass flux across $S_B^{\pm}$. That is, we impose the so-called diffuse-reflection boundary condition on $S_B^{\pm}$ [9].

(3) The gas molecules are reflected specularly on $S_{L1}^{\pm}$ and $S_{L2}^{\pm}$, that is, only the normal component to the boundary is inverted through the collision. Thus, the collisions between a gas molecule and $S_{Lj}^{\pm}$ ($j = 1, 2$) do not contribute to the drag force.

(4) The velocity V_B is the monotonically increasing function of t_*. This is expected to be true as long as $V_B(t_* = 0) < V_{B\infty}$ ([11,17,18]).

(5) The physical quantities are uniform in the X_3 direction.

Before we describe basic equations, let us summarize (and repeat) the notations used in the present paper: t_* is the time variable; $\boldsymbol{X}$ is the Cartesian coordinates in space; $\boldsymbol{\xi} = (\xi_1,\xi_2,\xi_3)$ is the molecular velocity; $X_B(t_*)$ is the position (in the X_1 direction) of the base plate; $V_B(t_*)$ is the velocity (in the X_1 direction) of the body; V_{B0} and $V_{B\infty}$ are, respectively, the initial and the terminal velocities; $f_*(X_1,X_2,\boldsymbol{\xi},t_*)$ is the molecular velocity distribution function; F_* is the constant external force per unit mass; G_* is the drag force; M_* is the mass of the body (G_* and M_* are defined for unit length in the X_3 direction); and H is the width of the lateral plates. Then we introduce the following dimensionless counterparts:

$$\begin{aligned} t &= t_*/t_0, \quad \boldsymbol{x} = \boldsymbol{X}/L, \quad \boldsymbol{\zeta} = \boldsymbol{\xi}/\xi_0, \\ x_B(t) &= X_B(t_*)/L, \quad v_B(t) = V_B(t_*)/\xi_0, \\ v_{B0} &= V_{B0}/\xi_0, \quad v_{B\infty} = V_{B\infty}/\xi_0, \\ f(\boldsymbol{x},\boldsymbol{\zeta},t) &= f_*(\boldsymbol{X}_*,\boldsymbol{\xi}_*,t_*)/\left(\rho_0\xi_0^{-3}\right), \\ F &= F_*/\left(Lt_0^{-2}\right), \quad G = G_*/\left(\rho_0 L^3 t_0^{-2}\right), \\ M &= M_*/(\rho_0 L^2), \quad h = H/L, \end{aligned} \tag{2}$$

where ρ_0 is the reference density of the gas, T_0 is the reference temperature of the gas (and is equal to the temperature of the body), L is the width of the base plate, $\xi_0 = (2R_0T_0)^{1/2}$ is the reference speed (R_0 is the specific gas constant), and $t_0 = L/\xi_0$ is the reference time. We further introduce the marginal velocity distribution function g as

$$g(x_1,x_2,\zeta_1,\zeta_2,t) = \int_{\mathbb{R}} f(x_1,x_2,\boldsymbol{\zeta},t)d\zeta_3. \tag{3}$$

B. Basic equations

The free transport equation that describes the behavior of the gas is written as

$$\frac{\partial g}{\partial t} + \zeta_1\frac{\partial g}{\partial x_1} + \zeta_2\frac{\partial g}{\partial x_2} = 0, \tag{4}$$

and the initial condition is

$$g = E(\zeta) \quad \text{at} \quad t = 0, \tag{5}$$

where $E(\zeta)$ is the equilibrium:

$$E(\zeta) = \pi^{-1}\exp(-\zeta^2), \quad \zeta = \left(\zeta_1^2+\zeta_2^2\right)^{1/2}. \tag{6}$$

The faces of the plates in the dimensionless form without the irrelevant x_3 component are

$$\mathsf{S}_B^{\pm}(t) = \{x_1 = x_B(t) \pm 0,\ x_2 \in [-1/2,1/2]\}, \tag{7a}$$

$$\mathsf{S}_{L1}^{\pm}(t) = \{x_1 \in [x_B(t),x_B(t)+h],\ x_2 = 1/2 \mp 0\}, \tag{7b}$$

$$\mathsf{S}_{L2}^{\pm}(t) = \{x_1 \in [x_B(t),x_B(t)+h],\ x_2 = -1/2 \pm 0\}. \tag{7c}$$

The boundary condition on the base plate is written as

$$g = g_{B\pm}(x_2,\zeta_1,\zeta_2,t) \quad \text{at} \quad (x_1,x_2)\in\mathsf{S}_B^{\pm}(t) \quad \text{for} \quad \zeta_1 \gtrless v_B(t), \tag{8}$$

where

$$g_{B\pm} = \pi^{-1}\sigma_{\pm}(x_2,t)\exp\left(-[\zeta_1 - v_B(t)]^2 - \zeta_2^2\right), \tag{9a}$$

$$\sigma_{\pm}(x_2,t) = \mp 2\pi^{1/2}\int_{\zeta_1 \lessgtr v_B(t)} [\zeta_1 - v_B(t)]g(x_1,x_2,\zeta_1,\zeta_2,t) \times d\zeta_1 d\zeta_2, \quad [(x_1,x_2)\in\mathsf{S}_B^{\pm}(t)]. \tag{9b}$$

The boundary conditions on the lateral plates 1 and 2 are, respectively,

$$g(x_1,x_2,\zeta_1,\zeta_2,t) = g(x_1,x_2,\zeta_1,-\zeta_2,t) \quad \text{at} \quad (x_1,x_2)\in\mathsf{S}_{L1}^{\pm} \quad \text{for} \quad \zeta_2 \lessgtr 0, \tag{10a}$$

$$g(x_1,x_2,\zeta_1,\zeta_2,t) = g(x_1,x_2,\zeta_1,-\zeta_2,t) \quad \text{at} \quad (x_1,x_2)\in\mathsf{S}_{L2}^{\pm} \quad \text{for} \quad \zeta_2 \gtrless 0. \tag{10b}$$

The position $x_B(t)$ and the velocity $v_B(t)$ of the body contained in Eqs. (4)–(10) are coupled with the equation of motion,

$$\frac{d}{dt}\begin{bmatrix} x_B(t) \\ v_B(t) \end{bmatrix} = \begin{bmatrix} v_B(t) \\ F - \frac{1}{M}G \end{bmatrix}, \quad \begin{bmatrix} x_B(0) \\ v_B(0) \end{bmatrix} = \begin{bmatrix} 0 \\ v_{B0} \end{bmatrix}. \tag{11}$$

The initial position can be set to zero without the loss of generality. The initial velocity v_{B0} is set to zero in the present paper since it was numerically shown in Ref. [18], where the body is convex, that the value of v_{B0} does not affect the overall behavior as long as $v_{B0} < v_{B\infty}$. As stated in Sec. II A, we treat only the case of $v_{B0} < v_{B\infty}$ in the present paper. The drag force G is determined through the velocity distribution function at $(x_1,x_2)\in\mathsf{S}_B^{\pm}$ as

$$G = G_+ + G_-, \tag{12a}$$

$$G_{\pm} = \pm\int_{-1/2}^{1/2}\left\{\iint_{\zeta_1 \lessgtr v_B(t)} [\zeta_1 - v_B(t)]^2 g(x_B(t)\pm 0,x_2,\zeta_1,\zeta_2,t) \times d\zeta_1 d\zeta_2 + \iint_{\zeta_1 \gtrless v_B(t)} [\zeta_1 - v_B(t)]^2 \times g_{B\pm}(x_2,\zeta_1,\zeta_2,t)d\zeta_1 d\zeta_2\right\}dx_2. \tag{12b}$$

The first term in the right-hand side of Eq. (12b) is the contribution from the molecules that impinge on $\mathsf{S}_B^{\pm}$ and the second term is the contribution from those reflected by $\mathsf{S}_B^{\pm}$. The velocity distribution of reflected molecules are determined by the use of Eq. (9).

Equations (4)–(10) for the gas and Eqs. (11) and (12) are the coupled system. To be more precise, it is a free boundary problem of the kinetic equation in two dimension for both space variables and molecular velocity variables. Moreover, we are interested in the long-time behavior. Such a class of the problem is difficult to solve in general, even without the collision term, for the following reasons:

(i) The unknown function g has five independent variables $(x_1,x_2,\zeta_1,\zeta_2,t)$.

(ii) The numerical solution needs to be extremely accurate to observe the rate of approach, since we treat the long-time behavior of the vanishing quantity $|v_{B\infty} - v_B(t)|$.

(iii) The velocity distribution function localizes in the velocity space for moving boundary problems [21,22]. For this

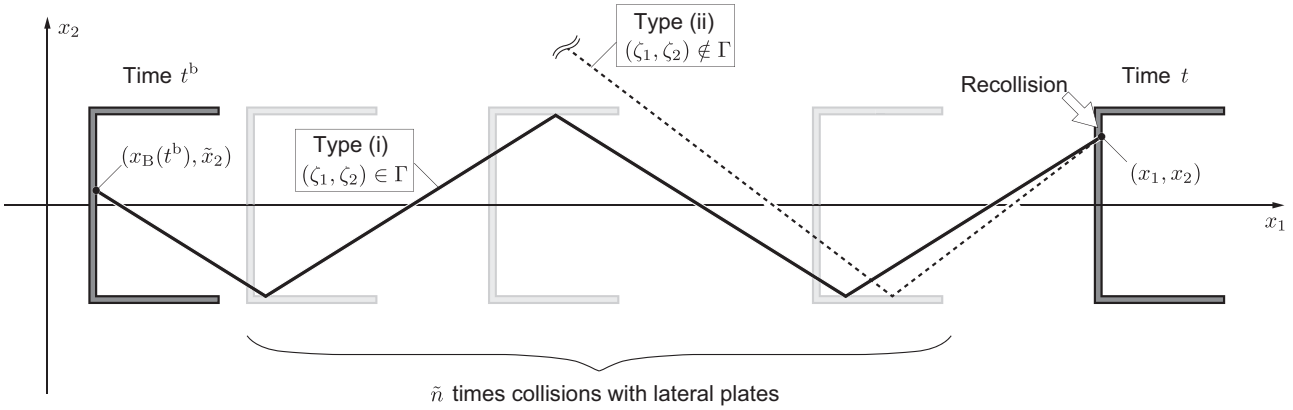

FIG. 2. Schematic description of $\Gamma = \Gamma_1 \times \Gamma_2$. Solid zigzag curve [type (i)] is the molecular path of the molecule that collides with the base plate at time t^b and time t (recollision). Dashed zigzag curve [type (ii)] is the molecular path of the molecule coming from the initial condition, i.e., $t^b = 0$.

reason, a standard finite-difference method or a finite-volume method loses the accuracy.

In addition to the above-mentioned known difficulties, the velocity distribution function is a piecewise continuous function in ζ_2 space as will be seen in Sec. V A 1. It is necessary for the accurate computation to capture the detailed structure of such velocity distribution function. Therefore, we solve the system Eqs. (4)–(11), extending the numerical method developed in the previous studies [18–21]. The method resolves all the difficulties mentioned above.

III. PRELIMINARY FOR THE NUMERICAL ANALYSIS

In order to solve the equation of motion (11), we need the drag (12). The velocity distribution function $g_{B\pm}$ in the second term of the right-hand side of (12b) is given by Eq. (9). Therefore, we notice that the velocity distribution function

$$g(x_1,x_2,\zeta_1,\zeta_2,t) \quad \text{at} \quad (x_1,x_2) \in \mathsf{S}_B^{\pm}(t) \quad \text{for} \quad \zeta_1 \lessgtr v_B(t), \quad \zeta_2 \in \mathbb{R}, \tag{13}$$

included in Eq. (9b) and the first term in the right-hand side of Eq. (12b) is all we have to compute to obtain the drag. We note that Eq. (13) is the velocity distribution function on the base plate with the impinging molecular velocities. First, we describe the method to compute σ_+ (9b) in Sec. III A and later σ_- and $G_\pm$ in Sec. III B.

A. Transformation of σ_+

The velocity distribution function is a constant along its characteristic curve, which is a trajectory of a molecule. In fact, a solution to Eq. (4) may be written as

$$g(x_1,x_2,\zeta_1,\zeta_2,t) = g\left(x_1^b,\tilde{x}_2,\zeta_1,(-1)^{\tilde{n}}\zeta_2,t^b\right), \tag{14a}$$

$$x_1^b = x_1 - \zeta_1(t - t^b), \tag{14b}$$

where $t^b \in [0,t]$ and $(x_1^b,\tilde{x}_2)$ are a time and a point at which the characteristic curve originates, and $\tilde{n}$ is the number of collisions between the lateral plates and the molecule. We call t^b the backward exit time. The expressions for t^b, $\tilde{x}_2$, and $\tilde{n}$ will be specified in Secs. III A 1 and III A 2. If we trace a molecular path back in time, we reach either (i) the base plate at time t^b or (ii) the initial time, i.e., $t^b = 0$ [see Fig. 2 in the case of $(x_1,x_2) \in \mathsf{S}_B^+(t)$]. In the latter case we immediately obtain $g = E$ [cf. Eq. (5)]. In contrast to the previous studies [18–21], the molecule may hit the lateral plates $\tilde{n}(\geqslant 0)$ times along the way. In such a case, we change the molecular velocity according to the specular reflection (10). When the molecule classified in type (i) collides with the base plate at a future time $t(>t^b)$, we say that the molecule *recollides* with the body (see Fig. 2). Let us introduce the set Γ_1 and Γ_2 so that the molecular velocity of the recolliding molecule is expressed as $\zeta_1 \in \Gamma_1$ and $\zeta_2 \in \Gamma_2$ [or $(\zeta_1,\zeta_2) \in \Gamma = \Gamma_1 \times \Gamma_2$]. By the use of Γ_1 and Γ_2, the quantity σ_+ (9b) is rewritten as

$$-\frac{\sigma_+}{2\pi^{1/2}} = \int_{-\infty}^{\infty}\int_{-\infty}^{v_B}[\zeta_1 - v_B(t)]E(\zeta)d\zeta_1 d\zeta_2 + \int_{\zeta_1\in\Gamma_1}\int_{\zeta_2\in\Gamma_2}[\zeta_1 - v_B(t)] \times [g_{B+}(\tilde{x}_2,\zeta_1,(-1)^{\tilde{n}}\zeta_2,t^b) - E(\zeta)]d\zeta_2 d\zeta_1. \tag{15}$$

The first term in the right-hand side is the quantity σ_+ obtained by neglecting the recollision, that is, by substituting $g = E$ into Eq. (9b). This term is explicitly computed in the last paragraph of Sec. III B. The second term is the correction by the recollision of molecules, whose molecular velocity is included in the set Γ. In the argument of g_{B+} in Eq. (15), $\tilde{x}_2$ is the position of the molecule at time t^b. In other words, the second term is the contribution of the molecules that leave a point $(x_B(t^b),\tilde{x}_2) \in \mathsf{S}_B^+(t^b)$ at a time t^b and impinge a point $(x_1,x_2) \in \mathsf{S}_B^+(t^b)$ at a time t (Fig. 2). We specify t^b, $\tilde{x}_2$, $\tilde{n}$, Γ_1, and Γ_2 in the following.

1. *Expressions of Γ_1 and t^b*

We describe the trajectory of the base plate in Fig. 3(a) in (x_1,t) plane. When the velocity of the body is monotonically increasing in time, the trajectory [the bold curve in Fig. 3(a)] is always convex upward. For a molecule to make recollision at time t, the necessary condition is

$$\zeta_1 \in \Gamma_1 = \{w(t) < \zeta_1 < v_B(t)\}, \quad w(t) = \frac{x_B(t)}{t}. \tag{16}$$

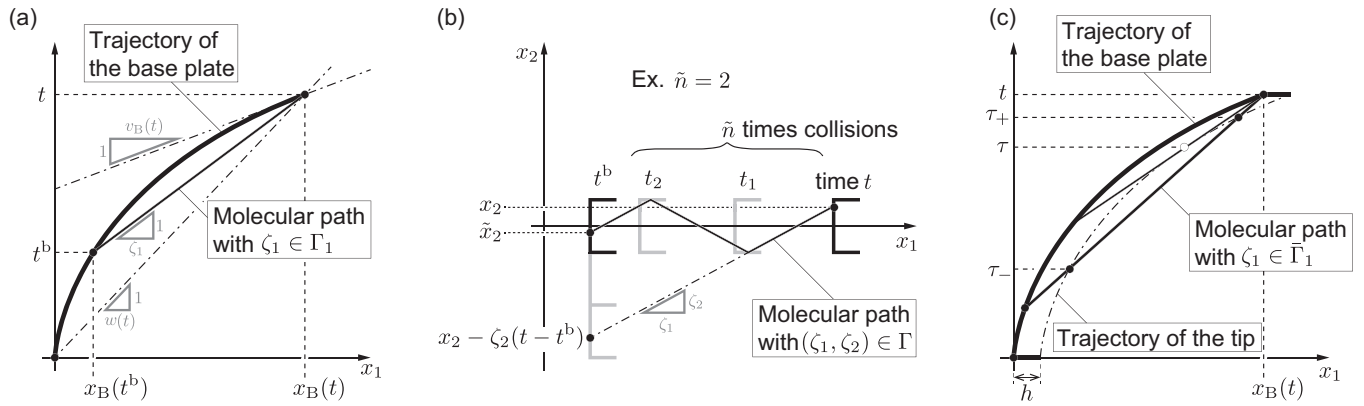

FIG. 3. Schematic diagrams for the definitions of (a) t^b and Γ_1; (b) $\tilde{x}_2$; and (c) $\bar{\Gamma}_1$, τ, and $\tau_\pm$.

The backward exit time t^b is defined as

$$t^b = \{{}^\exists\hat{t} \in [0,t] | x_B(t) - \zeta_1(t-\hat{t}) = x_B(\hat{t})\}. \quad (17)$$

2. Expressions of $\tilde{n}$ and $\tilde{x}_2$

In Fig. 3(b), we describe the schematic motion of the body in the (x_1,x_2) plane. The molecule makes recollision if $(\zeta_1,\zeta_2) \in \Gamma$. It collides with the lateral plates $\tilde{n}$ times, where $\tilde{n}$ is given by

$$\tilde{n} = \mp\left\lfloor x_2 - \zeta_2(t-t^b) + \tfrac{1}{2}\right\rfloor \quad \text{for} \quad \zeta_2 \gtrless 0. \quad (18)$$

Here $\lfloor X \rfloor$ is a floor function and takes the largest integer smaller than X. Using Eq. (18), the position $\tilde{x}_2$ is given by

$$\tilde{x}_2 = (-1)^{\tilde{n}}[x_2 - \zeta_2(t-t^b) \pm \tilde{n}] \quad \text{for} \quad \zeta_2 \gtrless 0. \quad (19)$$

3. Expression of Γ_2

We consider only the case of a positive ζ_2, since the case of a negative ζ_2 can be treated in the same manner. First, we note that Γ_2 is the function of ζ_1, and we divide Γ_1 into two parts as follows:

$$\Gamma_1 = \bar{\Gamma}_1 \cup \Gamma_1^\infty, \quad \bar{\Gamma}_1 = [w(t), v_B(\tau)), \quad \Gamma_1^\infty = [v_B(\tau), v_B(t)], \quad (20)$$

where a time τ is defined as

$$\tau = \{{}^\exists\hat{\tau} \in [0,t] | x_B(t) - v_B(\hat{\tau})(t-\hat{\tau}) = x_B(\hat{\tau}) + h, \; w(t) < v_B(\hat{\tau})\}. \quad (21)$$

The schematic diagram for the definitions of $\bar{\Gamma}_1$, Γ_1^∞, and τ are described in Fig. 3(c). The dash-dot curve in Fig. 3(c) is the trajectory of the tip, i.e., the right end of lateral plates (cf. Fig. 1). The molecules having the velocity in Γ_1^∞ never go outside of the concavity, since their x_1 components are always included in $[x_B, x_B + h]$. On the other hand, the molecules having the velocity in $\bar{\Gamma}_1$ stay outside of the body during the time interval $I_{\text{out}} = [\tau_-, \tau_+]$, where

$$\tau_- = \min\{{}^\exists\hat{\tau} \in [0,t] | x_B(t) - \zeta_1(t-\hat{\tau}) = x_B(\hat{\tau}) + h, \; \zeta_1 \in \bar{\Gamma}_1\}, \quad (22a)$$

$$\tau_+ = \max\{{}^\exists\hat{\tau} \in [0,t] | x_B(t) - \zeta_1(t-\hat{\tau}) = x_B(\hat{\tau}) + h, \; \zeta_1 \in \bar{\Gamma}_1\}. \quad (22b)$$

If such a molecule translates in the x_2 direction and $|x_2| > 1/2$ is satisfied during the time interval I_{out}, the molecule cannot recollide with the body in a future time regardless of ζ_1. That is, the molecular velocity for such a molecule should be excluded from Γ_2. Let us denote by t_k $(t_1 > t_2 > \cdots > t_k > \cdots > t_{\tilde{n}})$ the instants that a molecule hits the lateral plates [cf. Fig. 3(b)]:

$$t_k = t - \frac{x_2 + (2k-1)/2}{\zeta_2} \quad \text{for} \quad \zeta_2 > 0. \quad (23)$$

Then, for a molecule to recollide, all t_k must be outside of the interval I_{out}. Summarizing the above discussion, we have

$$\Gamma_2 = \begin{cases} \mathbb{R} & \text{for} \quad \zeta_1 \in \Gamma_1^\infty, \\ \bar{\Gamma}_2 = \{t_k \in [t^b, \tau_-] \cup [\tau_+, t], \; {}^\forall k = 1, \ldots, \tilde{n}\} & \text{for} \quad \zeta_1 \in \bar{\Gamma}_1. \end{cases} \quad (24)$$

Since it is not possible to have an explicit expression for $\bar{\Gamma}_2$, we compute $\bar{\Gamma}_2$ numerically. A recipe is shown in Appendix A, and we only give some comments in this section.

The set $\bar{\Gamma}_2$ turns out to be a series of discrete finite segments, and thus any function on $\bar{\Gamma}_2$ is piecewise continuous with finite supports. It is necessary to capture its shape in order for the accurate numerical integration of, e.g., Eq. (15). For a given set of F and h, there may not exist τ [Eq. (21)] for some t. In such a time t, we set $\Gamma_2 = \mathbb{R}$. If this is true for all t under concern (e.g., the case of $h \to \infty$), the problem is reduced to the case of an infinite plate as the body (see the case of $d = 1$ in Ref. [18]).

B. Transformation of σ_- and $G_\pm$

In the present problem, the trajectory of the body is convex upward in (x_1,t) space as shown in Fig. 3(a). The recollision on the back of the body S_B^- never happens in such a case. Therefore, we can substitute $g = E$ into Eq. (9b) to obtain

$$\sigma_- = 2\pi^{1/2}\int_{-\infty}^{\infty}\int_{v_B(t)}^{\infty}[\zeta_1 - v_B(t)]E(\zeta)d\zeta_1 d\zeta_2. \tag{25}$$

The first term of the drag force (12b) has a form similar to $\sigma_\pm$, and thus it follows by the same argument in Sec. III A that

$$G_+ = \int_{-1/2}^{1/2}\left\{\int_{-\infty}^{\infty}\int_{-\infty}^{v_B}[\zeta_1 - v_B(t)]^2E(\zeta)d\zeta_1 d\zeta_2 + \int_{\zeta_1\in\Gamma_1}\int_{\zeta_2\in\Gamma_2}[\zeta_1 - v_B(t)]^2[g_{B+}(\tilde{x}_2,\zeta_1,(-1)^{\tilde{n}}\zeta_2,t^b) - E(\zeta)]d\zeta_2 d\zeta_1 \right.$$
$$\left. + \int_{-\infty}^{\infty}\int_{v_B}^{\infty}[\zeta_1 - v_B(t)]^2 g_{B+}(x_2,\zeta_1,\zeta_2,t)d\zeta_1 d\zeta_2\right\}dx_2, \tag{26a}$$

$$G_- = -\int_{-1/2}^{1/2}\left\{\int_{-\infty}^{\infty}\int_{v_B}^{\infty}[\zeta_1 - v_B(t)]^2E(\zeta)d\zeta_1 d\zeta_2 + \int_{-\infty}^{\infty}\int_{-\infty}^{v_B}[\zeta_1 - v_B(t)]^2 g_{B-}(x_2,\zeta_1,\zeta_2,t)d\zeta_1 d\zeta_2\right\}dx_2. \tag{26b}$$

Some integrals included in Eqs. (15), (25), and (26) can be explicitly carried out. The integral in the first term of Eqs. (15) and (25) is

$$\iint_{\zeta_1\lessgtr v_B}(\zeta_1 - v_B)Ed\zeta_1 d\zeta_2 = -\frac{1}{2}\left[v_B \pm \frac{e^{-v_B^2}}{\sqrt{\pi}} \pm v_B\mathrm{erf}(v_B)\right], \tag{27}$$

and that in the first terms of Eqs. (26a) and (26b) is

$$\iint_{\zeta_1\lessgtr v_B}(\zeta_1 - v_B)^2Ed\zeta_1 d\zeta_2 = \frac{1}{2}\left(v_B^2 + \frac{1}{2}\right)[1 \pm \mathrm{erf}(v_B)] \pm \frac{v_B e^{-v_B^2}}{2\sqrt{\pi}}, \tag{28}$$

where $\mathrm{erf}(v_B)$ is the error function. Finally, the integral in the last term of Eqs. (26a) and (26b) is

$$\iint_{\zeta_1\gtrless v_B}(\zeta_1 - v_B)^2 g_{B\pm}d\zeta_1 d\zeta_2 = \frac{\sigma_\pm}{4}. \tag{29}$$

IV. NUMERICAL METHOD

After the preliminary analysis in Sec. III, our problem is reduced to the equation of motion (11) with the drag (26), supplemented by Eqs. (15), (25), and (27)–(29). This is an ordinary differential equation with a history term [the integrals for $(\zeta_1,\zeta_2) \in \Gamma_1 \times \Gamma_2$ in Eqs. (15) and (26a)], that includes the displacement x_B and the velocity v_B in the past time t^b. We denote the history terms by $\mathcal{H}_p$ [cf. Eqs. (15) and (26a)]:

$$\mathcal{H}_p(x_2,t) = \int_{\Gamma_1}\bar{Q}_p(x_2,\zeta_1,t)d\zeta_1, \tag{30a}$$

$$\bar{Q}_p(x_2,\zeta_1,t) = \int_{\Gamma_2}Q_p(x_2,\zeta_1,\zeta_2,t)d\zeta_2, \tag{30b}$$

$$Q_p(x_2,\zeta_1,\zeta_2,t) = [\zeta_1 - v_B(t)]^p\mathcal{Q}(x_2,\zeta_1,\zeta_2,t), \tag{30c}$$

$$\mathcal{Q}(x_2,\zeta_1,\zeta_2,t) = g_{B+}(\tilde{x}_2,\zeta_1,(-1)^{\tilde{n}}\zeta_2,t^b) - E(\zeta), \tag{30d}$$

where $p = 1$ or 2; $\tilde{x}_2$ and t^b are defined by, respectively, Eqs. (19) and (17). Equation (30d) is the velocity distribution function of the recolliding molecules minus the velocity distribution function at the equilibrium. Therefore, we call $\mathcal{Q}$ the correction by recollision. The ordinary differential equation with the history term is solved numerically in a standard manner, that is, we apply the third-order Adams-Bashforth method for Eq. (11) and the trapezoidal approximation for the integrals in the history terms. However, special care is taken to obtain Γ.

A. Discretization

Let us introduce the following discretized independent variables: $t^{(m)} = m\Delta t$, $x_2^{(j)} = j\Delta x_2$, $\zeta_1^{(k)} = \mathcal{L}_1(k)$ [cf. Eq. (32)], and $\zeta_2^{(l)} = \mathcal{L}_2(l)$ [cf. Eqs. (33) and (34)], where m is a step number ($m = 0,1,\ldots$), Δt is a time step, $\Delta x_2 = (2N_{x_2})^{-1}$ is a grid size in space, and N_{x_2} is the number of the grid ($j = -N_{x_2},\ldots,N_{x_2}$). The grid in the velocity variables, $\mathcal{L}_1$ and $\mathcal{L}_2$, will be specified in Sec. IV B. These are defined in such a way that the grid system in (ζ_1,ζ_2) adopts the range of integral Γ [cf. Eqs. (16) and (24)].

Note that $\mathcal{L}_1$ is dependent on $t^{(m)}$ and $\mathcal{L}_2$ is dependent on $x_2^{(j)}$, $\zeta_1^{(k)}$, $t^{(m)}$; however, their dependencies are not explicitly shown. The dependent variables are discretized as $x_B^{(m)} = x_B(t^{(m)})$, $v_B^{(m)} = v_B(t^{(m)})$, $G_\pm^{(m)} = G_\pm(t^{(m)})$, and $\sigma_\pm^{(j,m)} = \sigma_\pm(x_2^{(j)},t^{(m)})$. Using the third-order Adams-Bashforth method, the equation of motion (11) is discretized as

$$\begin{aligned} x_B^{(m+1)} &= x_B^{(m)} + \Delta t \sum_{m'=0}^{2} W_{\mathrm{AB}}^{(m')} v_B^{(m-m')}, \\ v_B^{(m+1)} &= v_B^{(m)} + \Delta t \sum_{m'=0}^{2} W_{\mathrm{AB}}^{(m')} \left[F - \frac{1}{M}(G_+^{(m-m')} + G_-^{(m-m')}) \right], \end{aligned} \quad \text{for} \quad m = 2,3,\ldots, \tag{31}$$

with weights $W_{\mathrm{AB}}^{(m')}$ given by $W_{\mathrm{AB}}^{(0)} = 23/12$, $W_{\mathrm{AB}}^{(1)} = -4/3$, and $W_{\mathrm{AB}}^{(2)} = 5/12$, where suitable lower-order schemes are applied for $m = 0$ and $m = 1$. The initial conditions are $x_B^{(0)} = 0$ and $v_B^{(0)} = 0$. Substituting $v_B^{(0)} = 0$ into Eqs. (15), (25), and (26), we obtain $\sigma_\pm^{(0)} = 1$ and $G_\pm^{(0)} = \pm 1/2$. In the drag force $G_\pm^{(m)}$, all the terms can be explicitly computed as soon as $v_B^{(m)}$ is obtained, except for the history terms: $\mathcal{H}_p^{(j,m)} = \mathcal{H}_p(x_2^{(j)},t^{(m)})$, $\bar{Q}_p^{(j,k,m)} = \bar{Q}_p(x_2^{(j)},\zeta_1^{(k)},t^{(m)})$, and $Q_p^{(j,k,l,m)} = Q_p(x_2^{(j)},\zeta_1^{(k)},\zeta_2^{(l)},t^{(m)})$. The next section, Sec. IV B, is devoted to describing the computational method for these terms.

The numerical algorithms to obtain t^b, τ, and $\tau_\pm$, which are necessary to carry out the computation in Sec. IV B, are described in Appendix B. Moreover, the functions with these arguments, i.e., the values $v_B(t^b)$ and $\sigma_+(\tilde{x}_2,t^b)$, which are not on the grid points, are linearly interpolated by using neighbor discrete points.

B. Integration of the history term

Let us begin with the integration with respect to ζ_1 [Eq. (30a)]. Since the range of integration Γ_1 [Eq. (20)] is dependent on $t^{(m)}$, we discretize $\zeta_1 \in \Gamma_1(t) = \Gamma_1^\infty \cup \bar{\Gamma}_1$ in the following manner. First, we replace $v_B(t)$ and $v_B(\tau)$ by, respectively, $\check{v}_{B,t} = (x_B^{(m)} - x_B^{(m-1)})/\Delta t$ and $\check{v}_{B,\tau}$ [cf. a sentence below Eq. (B4) in Appendix B]. We introduce the minimum grid size $\Delta\zeta_{1\,\mathrm{min}}$ and the minimum number of grid $N_{1\,\mathrm{min}}$ and define the total number of grid points for $\bar{\Gamma}_1$ and Γ_1^∞, respectively, as $\bar{N}_1 = \max\left(\lceil \frac{\check{v}_{B,\tau} - w(t^{(m)})}{\Delta\zeta_{1\,\mathrm{min}}} \rceil, N_{1\,\mathrm{min}}\right)$ and $N_1^\infty = \max\left(\lceil \frac{\check{v}_{B,t} - \check{v}_{B,\tau}}{\Delta\zeta_{1\,\mathrm{min}}} \rceil, N_{1\,\mathrm{min}}\right)$, where $\lceil X \rceil$ is the ceil function that takes the smallest integer larger than X. Using these values and $N_1 = \bar{N}_1 + N_1^\infty$, we determine $\mathcal{L}_1(k)$ as

$$\mathcal{L}_1(k) = \begin{cases} w(t^{(m)}) + [\check{v}_{B,\tau} - w(t^{(m)})]\left[1 - \frac{(\bar{N}_1 - k)^{n_p}}{\bar{N}_1^{n_p}}\right] & \text{for} \quad k = 0,\ldots,\bar{N}_1 - 1, \\ \check{v}_{B,\tau} - (\check{v}_{B,t} - \check{v}_{B,\tau})\left(\frac{\bar{N}_1 - k}{N_1^\infty}\right) & \text{for} \quad k = \bar{N}_1,\ldots,N_1, \end{cases} \tag{32}$$

where n_p is set to 5 unless otherwise stated. By choosing larger n_p, the grid points are accumulated near the velocity $\check{v}_{B,\tau}$. Note that $n_p = 1$ leads to uniform meshing for $k = 0,\ldots,\bar{N}_1 - 1$. By the use of Eq. (32), $\mathcal{H}_p^{(j,m)}$ is given by $\mathcal{H}_p^{(j,m)} = \sum_{k=0}^{N_1} \bar{Q}_p^{(j,k,m)} W_1^{(k)}$, where $W_1^{(k)}$ is the weight determined by a quadrature. We apply a trapezoidal rule as the quadrature through the present paper.

Next we describe the integration with respect to ζ_2 [Eq. (30b)]. Note that Γ_2 is dependent not only on $t^{(m)}$ but also on $\zeta_1^{(k)}$ [cf. Eq. (24)]. For $\zeta_1 \in \Gamma_1^\infty$, i.e., $k = \bar{N}_1,\ldots,N_1$, we have $\Gamma_2 = \mathbb{R}$. In such a case, we replace $\mathbb{R}$ by $[-Z,Z]$, where Z is the numerical parameter of truncation. Introducing the minimum grid size $\Delta\zeta_{2\,\mathrm{min}}$ and the minimum number of grid $N_{2\,\mathrm{min}}$, the number of grid points is $N_2 = \max\left(\lceil \frac{2Z}{\Delta\zeta_{2\,\mathrm{min}}} \rceil, N_{2\,\mathrm{min}}\right)$, and the grid function $\mathcal{L}_2$ is

$$\mathcal{L}_2(l) = -Z + \frac{2Z}{N_2} l, \quad \text{for} \quad l = 0,\ldots,N_2 \quad \text{and} \quad k = \bar{N}_1,\ldots,N_1. \tag{33}$$

Then $\bar{Q}_p^{(j,k,m)}$ is given by $\bar{Q}_p^{(j,k,m)} = \sum_{l=0}^{N_2} Q_p^{(j,k,l,m)} W_2^{(l)}$ for $k = \bar{N}_1,\ldots,N_1$, where $W_2^{(l)}$ is the weight determined by a quadrature.

On the other hand, for $\zeta_1 \in \bar{\Gamma}_1$, i.e., $k = 0,\ldots,\bar{N}_1 - 1$, we have $\Gamma_2 = \bar{\Gamma}_2$. According to the discussion in Appendix A, the range of integration $\bar{\Gamma}_2$ consists of $i_{\max}$ segments. To be more specific, $\bar{\Gamma}_2 = \bigcup_{i=1,\ldots,i_{\max}} [\zeta_{2\,\mathrm{min}}^{(i)}, \zeta_{2\,\mathrm{max}}^{(i)}]$, where $\zeta_{2\,\mathrm{min}}^{(i)}$ and $\zeta_{2\,\mathrm{max}}^{(i)}$ are obtained numerically using the recipe in Appendix A. For each segment, the number of grid points is $N_2^{(i)} = \max\left(\lceil \frac{\zeta_{2\,\mathrm{max}}^{(i)} - \zeta_{2\,\mathrm{min}}^{(i)}}{\Delta\zeta_{2\,\mathrm{min}}} \rceil, N_{2\,\mathrm{min}}\right)$ and the grid function $\mathcal{L}_2$ is written as

$$\mathcal{L}_2(l) = \zeta_{2\,\mathrm{min}}^{(i)} + \left[\frac{\zeta_{2\,\mathrm{max}}^{(i)} - \zeta_{2\,\mathrm{min}}^{(i)}}{N_2^{(i)}}\right] l, \quad \text{for} \quad l = 0,\ldots,N_2^{(i)}, \quad k = 0,\ldots,\bar{N}_1, \quad \text{and} \quad i = 1,\ldots,i_{\max}. \tag{34}$$

Then $\bar{Q}_p^{(j,k,m)}$ is given by $\bar{Q}_p^{(j,k,m)} = \sum_{i=1}^{i_{\max}} [\sum_{l=0}^{N_2^{(i)}} Q_p^{(j,k,l,m)} W_2^{(l,i)}]$ for $k = 0,\ldots,\bar{N}_1 - 1$, where $W_2^{(l,i)}$ is the weight determined by a quadrature.

Finally, in Eq. (26a), the spatial integration is also necessary. This is approximated as $\int_{-1/2}^{1/2} \mathcal{H}_2(x_2,t)dx_2 = \sum_{j=-N_{x_2}}^{N_{x_2}} \mathcal{H}_2^{(j,m)} W_{x_2}^{(j)}$, where $W_{x_2}^{(l,i)}$ is the weight determined by a quadrature.

V. RESULT

Before presenting numerical results, we describe the parameters used in the numerical analysis. The (nondimensional) mass M is set to $M = 1$ throughout the paper because the

computation with $M = 1$ is identical to that with $M = M'$, $t = M't'$, and $F = F'/M'$. The external force F and the terminal velocity $v_{B\infty}$ are related each other as follows. As time goes to infinity, the velocity approaches the terminal velocity, for which the drag G/M counterbalances the external force F. For such a steady motion with the constant velocity $v_{B\infty}$, the recollision never happens, and thus the drag G can be explicitly expressed by using Eqs. (26a) with $\Gamma_1 = \Gamma_2 = \emptyset$ and (26b) together with (27)–(29), where $\sigma_\pm$ is obtained by Eqs. (15) with $\Gamma_1 = \Gamma_2 = \emptyset$ and (25). Therefore, in the actual numerical analysis, we set $v_{B\infty}$ rather than F and determine the corresponding F from these equations.

In the present problem, we are mainly concerned with the behavior of the difference

$$v_d(t) = |v_{B\infty} - v_B(t)|, \tag{35}$$

which is a monotonically decreasing function of time and vanishes in the limit of $t \to \infty$. In order to obtain vanishingly decreasing v_d with great accuracy, it is better to compute with the quadruple precision. Therefore, the external force F is also set with quadruple precision, e.g., $F = 6.27207102884489538488454807830 02$ for $v_{B\infty} = 2$.

As mentioned in Sec. I, v_d is expected to be in proportion to the inverse power of time. In order to examine this behavior in detail, we introduce the functional $\alpha(\mathcal{X})$ as

$$\alpha(\mathcal{X}) = \frac{d\log\mathcal{X}}{d\log t} \quad \text{for} \quad \mathcal{X} > 0, \tag{36}$$

where $\mathcal{X}$ is a time-dependent quantity. If $\alpha(\mathcal{X})$ approaches a constant as time goes to infinity, e.g., $\lim_{t\to\infty}\alpha(\mathcal{X}) \to n_*$, we may conclude $\mathcal{X} \approx Ct^{n_*}$ for sufficiently large t with C a positive constant.

Numerical parameters are set to

$$\Delta t = 0.05, \quad N_{x_2} = 4, \quad \Delta\zeta_{1\,\min} = 0.1, \quad N_{1\,\min} = 10,$$
$$\Delta\zeta_{2\,\min} = 0.1, \quad N_{2\,\min} = 4, \quad Z = 5, \tag{37}$$

unless otherwise stated. The error estimate using different values of numerical parameters are presented in Sec. V C.

A. Contribution of recolliding molecules

1. Velocity distribution function

We first visualize the contribution by recollision at the level of the velocity distribution function. Let us introduce the normalized molecular velocity as $\zeta_1^{\rm nor} = [\zeta_1 - w(t)]/[\check{v}_{B,t} - w(t)]$. Note that $\zeta_1^{\rm nor} \in [0,1]$ when $\zeta_1 \in \Gamma_1$. We show in Fig. 4 the velocity distribution function $\mathcal{Q}$ [cf. Eq. (30d)] versus $\zeta_2(>0)$ at $x_2 = 0$ for several values of $\zeta_1^{\rm nor} \in [0,1]$ and for (a) $t = 0.8$, (b) $t = 1, \ldots,$ (i) $t = 50$ in the case of $v_{B\infty} = 2$ and $h = 0.1$. The red curve represents $\mathcal{Q}$ with $\zeta_1^{\rm nor} = \check{v}_{B,\tau}^{\rm nor} \equiv [\check{v}_{B,\tau} - w(t)]/[\check{v}_{B,t} - w(t)]$ [cf. Eq. (21) and Fig. 3(c)]. First, let us focus on Fig. 4(a) at $t = 0.8$. The molecule with $\zeta_1^{\rm nor} > \check{v}_{B,\tau}^{\rm nor}$ is trapped by the concave part throughout its flight during the previous collision at time t^b and the present collision at time t. In other words, the x_1 component of the molecule never exceeds the x_1 component of the tip, i.e., $x_B + h$. The set Γ_2 for such a molecule is $\mathbb{R}$ and the curves are continuous for $\zeta_1^{\rm nor} > \check{v}_{B,\tau}^{\rm nor}$. However, the molecule with $\zeta_1^{\rm nor} < \check{v}_{B,\tau}^{\rm nor}$ has a chance to escape from the concave part during the previous collision at time t^b and the present collision at time t, since there exists a nonzero time interval during which the molecule is distant more than h from the base plate. If the molecular velocity ζ_2 of such a molecule is not included in Γ_2, the contribution by recollision is zero because it does not recollide. Therefore, the velocity distribution function for a certain $\zeta_1^{\rm nor}(<\check{v}_{B,\tau}^{\rm nor})$ is a piecewise continuous function with discrete supports. As time goes on [see Figs. 4(a) → 4(i)], the velocity distribution function changes such that $\check{v}_{B,\tau}^{\rm nor}$ increases and the velocity distribution function for $\zeta_1^{\rm nor} < \check{v}_{B,\tau}^{\rm nor}$ becomes a complex shape. In particular, the number of supports of the velocity distribution function depends on $\zeta_1^{\rm nor}$; the number is smaller for smaller $\zeta_1^{\rm nor}$ (e.g., the number is 1 for $\zeta_1^{\rm nor} = 0$) and the number becomes larger as $\zeta_1^{\rm nor}$ approaches $\check{v}_{B,\tau}^{\rm nor}$. Moreover, each support for a certain $\zeta_1^{\rm nor}$ shrinks as time goes on, as clearly demonstrated by the magnified figures of Figs. 4(g)–4(i). Note that we can accurately describe the velocity distribution of such a complex shape thanks to the numerical method described in the present paper.

We should mention how the velocity distribution function behaves in the two limits: $h \to \infty$ and $h \to 0$. In order to illustrate these two limits, we show in Fig. 5 the cases of $h = 10^3$ [Fig. 5(a)] and $h = 10^{-5}$ [Fig. 5(b)] at $x_2 = 0$ and $t = 5$. In the former case, most of the recolliding molecules are trapped in the concave part. On the other hand, in the latter case, most of recolliding molecules never experience a collision with lateral plates, and thus their ζ_2 is restricted to near $\zeta_2 \approx 0$ except for $\zeta_1^{\rm nor} \approx 1$. Note that $\check{v}_{B,\tau}^{\rm nor} \approx 1$ and the number of support is only one in this case. As Figs. 4 and 5 describe, the velocity distribution function varies qualitatively for different h. Since the velocity distribution function $\mathcal{Q}$ plays a key role in determining the rate of approach, we show some integrated quantities in the following.

2. Moments of $\mathcal{Q}$

In Fig. 6, a quantity described by Eq. (30b) with $p = 2$, which is the moment of $\mathcal{Q}$, is plotted against $\zeta_1^{\rm nor}$ for various t. The parameters are set to $v_{B\infty} = 2$ and $h = 0.1$. Let us first focus on Fig. 6(a). The moment $\bar{\mathcal{Q}}_2$ decreases as time goes on, however, there appears a sharp point (e.g., $\zeta_1^{\rm nor} \approx 0.4$ and $t = 1$), at which the velocity is $\zeta_1^{\rm nor} = \check{v}_{B,\tau}^{\rm nor}$. The occurrence of the sharp point is consistent with the observation of Fig. 4(b), in which the change of the velocity distribution function with respect to $\zeta_1^{\rm nor}$ shows different trends for $\zeta_1^{\rm nor} < \check{v}_{B,\tau}^{\rm nor}$ and $\zeta_1^{\rm nor} > \check{v}_{B,\tau}^{\rm nor}$. For larger times [see Figs. 6(b) → 6(d)], it seems that the moment $\bar{\mathcal{Q}}_2$ decreases nonuniformly in $\zeta_1^{\rm nor}$, and the sharp point becomes much sharper as time goes on. Figure 6 indicates that the $\bar{\mathcal{Q}}_2$ can be decomposed into two parts that have different long-time behaviors: $\bar{\mathcal{Q}}_2$ for $\zeta_1^{\rm nor} \in [\check{v}_{B,\tau}^{\rm nor}, 1]$ (or $\zeta_1 \in \Gamma_1^\infty$) and $\bar{\mathcal{Q}}_2$ for $\zeta_1^{\rm nor} \in [0, \check{v}_{B,\tau}^{\rm nor}]$ (or $\zeta_1 \in \bar{\Gamma}_1$). Therefore, it is natural to evaluate the history term by decomposing it into two parts: $\mathcal{H}_2 = \mathcal{H}_2^\infty + \bar{\mathcal{H}}_2$ with $\mathcal{H}_2^\infty = \int_{\Gamma_1^\infty} \bar{\mathcal{Q}}_2(x_2,\zeta_1,t)d\zeta_1$ and $\bar{\mathcal{H}}_2 = \int_{\bar{\Gamma}_1} \bar{\mathcal{Q}}_2(x_2,\zeta_1,t)d\zeta_1$.

The history term $\mathcal{H}_2$ for cases $h \to \infty$, $h = 0.1$, and $h \to 0$ are presented in Fig. 7(a) by solid curves. In the cases of $h > 0$, $\mathcal{H}_2$ decreases in proportion to t^{-3}, whereas $\mathcal{H}_2$ is proportional to t^{-4} for $h \to 0$. This observation is verified in Fig. 7(b), where the gradient α are shown for each curve. The decomposed parts for the case of $h = 0.1$ in Fig. 7, expressed

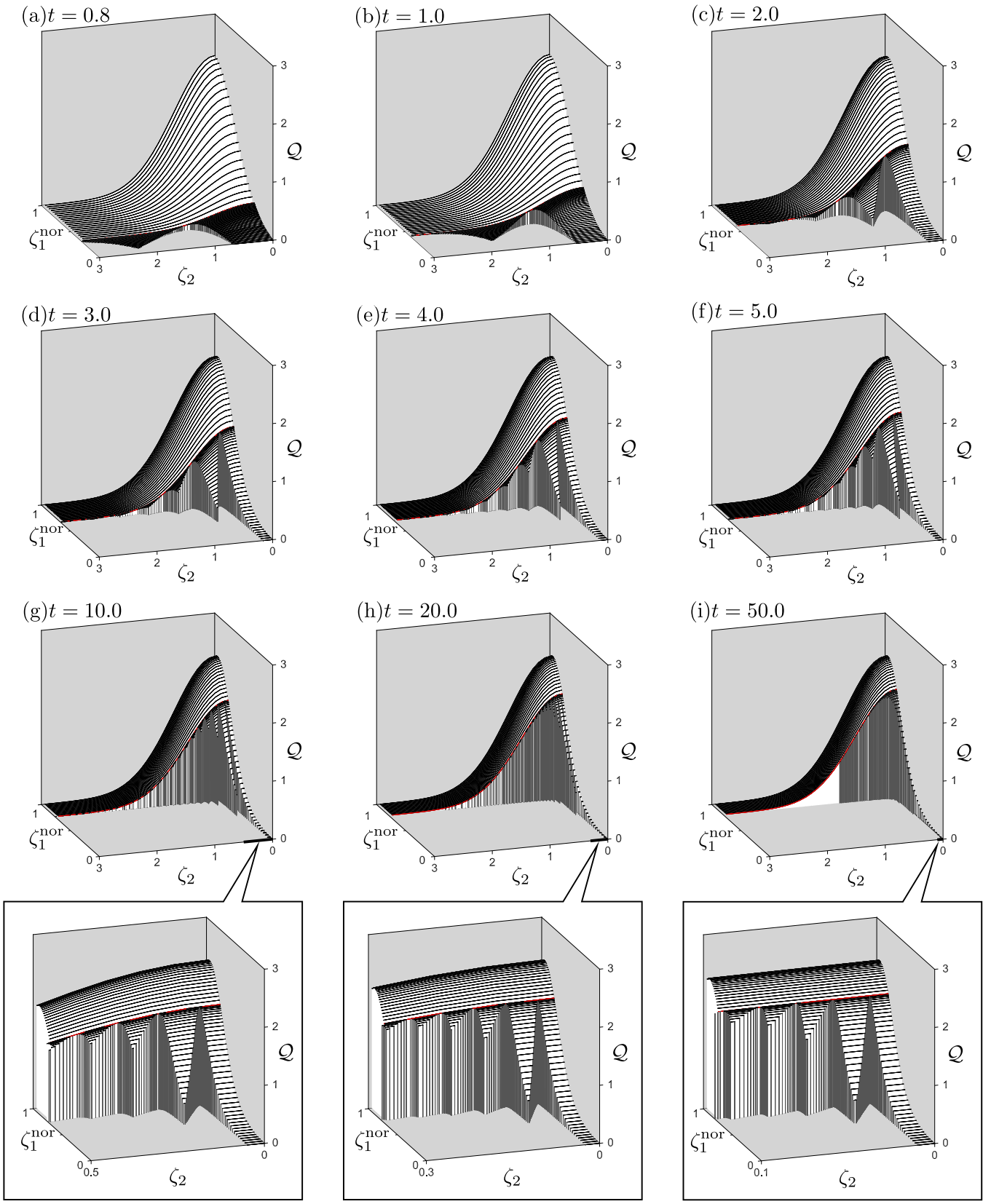

FIG. 4. (Color online) The velocity distribution function $\mathcal{Q}$ [cf. Eq. (30d)] versus $\zeta_2(>0)$ for several $\zeta_1^{\rm nor}$ at $x_2 = 0$ and time (a) $t = 0.8$, (b) $t = 1$, (c) $t = 2$, (d) $t = 3$, (e) $t = 4$, (f) $t = 5$, (g) $t = 10$, (h) $t = 20$, and (i) $t = 50$ in the case of $v_{B\infty} = 2$ and $h = 0.1$. The red (dark gray) curve represents $\mathcal{Q}$ with $\zeta_1^{\rm nor} = \check{v}_{B,\tau}^{\rm nor}$ [cf. Eq. (21) and Fig. 3(c)]. The magnified figure around $\zeta_2 \approx 0$ for (g)–(i) is also shown at the bottom row. For the better visualization, we set $n_p = 2$ and $N_{1\,\rm min} = 40$.

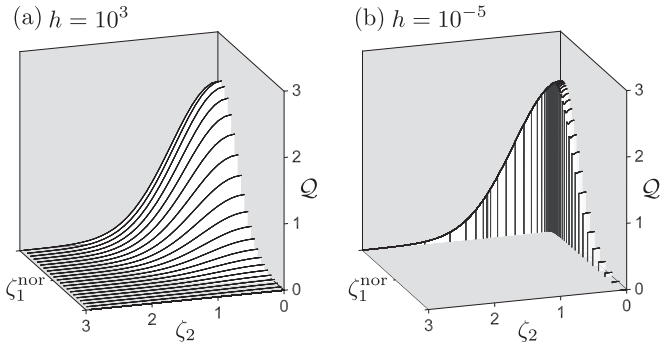

FIG. 5. The velocity distribution function $\mathcal{Q}$ [cf. Eq. (30d)] versus $\zeta_2(>0)$ for several $\zeta_1^{\rm nor}$ at $x_2 = 0$ and time $t = 5$. (a) $h = 10^3$ and (b) $h = 10^{-5}$ in the case of $v_{B\infty} = 2$ and $h = 0.1$. For better visualization, we set $N_{1\,\rm min} = 40$.

by dashed and dash-dot curves, show more details about the history term for finite h. To be specific, the contribution $\mathcal{H}_2^\infty$ from the molecules with velocity $\zeta_1^{\rm nor} > \check{v}_{B,\tau}^{\rm nor}$ decreases in proportion to t^{-3} for sufficiently large t (say, $t > 10^2$). In contrast, the contribution $\bar{\mathcal{H}}_2$ from the molecules with velocity $\zeta_1^{\rm nor} < \check{v}_{B,\tau}^{\rm nor}$ is seemingly proportional to t^{-4}. In Fig. 7(b), the gradient $\alpha(\bar{\mathcal{H}}_2)$ stays close to -4; however, the convergence is worse compared with other curves. We also show the result obtained by the finer grid $N_{1\,\rm min} = 40$ (solid), and it is seen the results is much closer to -4. In any case, the contribution from

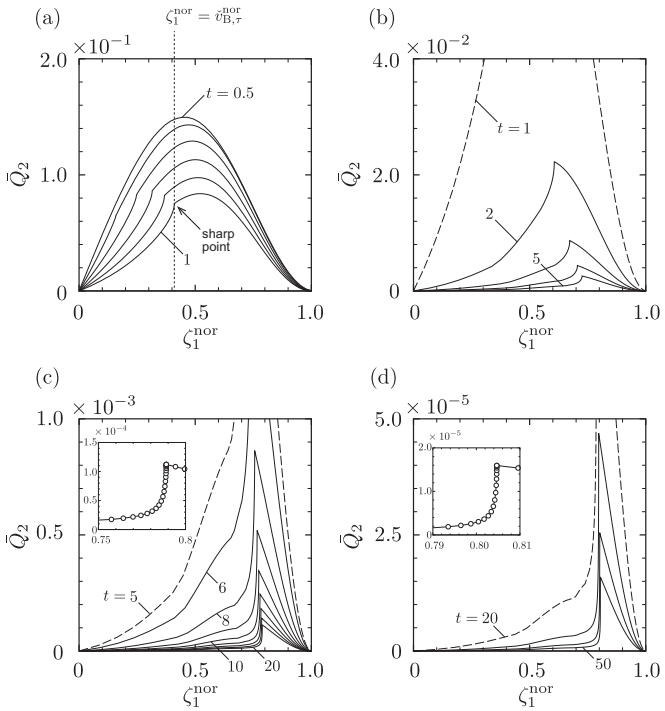

FIG. 6. The profile of $\bar{Q}_2$ versus $\zeta_1^{\rm nor}$ at $x_2 = 0$ and for various t in the case of $v_{B\infty} = 2$ and $h = 0.1$. (a) $t = 0.5, 0.6, \ldots, 1$; (b) $t = 1$ (dashed) and $t = 2, 3, 4, 5$ (solid); (c) $t = 5$ (dashed) and $t = 6, 8, \ldots, 20$ (solid); (d) $t = 20$ (dashed) and $t = 30, 40, 50$ (solid). In panels (c) and (d), the magnified figures around $\zeta_1^{\rm nor} \approx \check{v}_{B,\tau}^{\rm nor}$ are shown in the insets with circles at the grid points. For better visualization, we set $N_{1\,\rm min} = 40$.

$\zeta_1^{\rm nor} > \check{v}_{B,\tau}^{\rm nor}$ dominates the one from $\zeta_1^{\rm nor} < \check{v}_{B,\tau}^{\rm nor}$ for sufficiently large t.

B. Long-time behavior

Before presenting the results, recall that the rate of approach is described by $v_d \sim t^{-3}$ for $t \gg 1$ if $h = 0$ [18]. In Fig. 8, we show the long-time behavior of v_d. The bold curves are the results for the two limiting cases: $h \to \infty$ and $h \to 0$. As in the previous work [18], we observe the inverse power-law decay of $v_d \approx C_\infty t^{-2}$ for $h \to \infty$ and $v_d \approx C_0 t^{-3}$ for $h \to 0$, where C_∞ and C_0 are some positive constants. In between these two curves, the results of the cases with $h = 1 \times 10^{-1}$, 5×10^{-2}, 2.5×10^{-2} (dashed), 1×10^{-2}, 5×10^{-3}, 2.5×10^{-3} (long-dashed), 1×10^{-3}, 5×10^{-4}, and 2.5×10^{-4} (dash-dot) are plotted. It seems that the cases with $h = 1 \times 10^{-1}$, 5×10^{-2}, 2.5×10^{-2} exhibits the inverse power law t^{-2} for $t > 10$ as in the case of $h \to \infty$. On the other hand, the exponent of the power law is unclear for the cases with $h < 10^{-2}$. Therefore, we show in Fig. 8(b) the gradient of curves in Fig. 8(a), i.e., $\alpha(v_d)$. Moreover, we present $-\alpha(v_d) - 2$ [or $-\alpha(v_d) - 3$] in Fig. 8(c) [or Fig. 8(d)] in order to facilitate the visibility of approach of $\alpha(v_d)$ to -2 (or -3). From these figures, one can tell that the gradients for $h \to \infty$ (or $h \to 0$) obviously approach -2 (or -3). The differences are of the order of 10^{-3} at $t = 2 \times 10^3$, i.e., $-2 > \alpha(v_d) > -2.001$ for $h \to \infty$ [or $-3 > \alpha(v_d) \gtrsim -3.001$ for $h \to 0$]. In addition, we can see that $\alpha(v_d) \approx -2 - C_{\alpha\infty} t^{-1}$ for $h \to \infty$ and $\alpha(v_d) \approx -3 - C_{\alpha 0} t^{-1}$ for $h \to 0$, where $C_{\alpha\infty}$ and $C_{\alpha 0}$ are positive constants. In the cases of $0 < h < \infty$, we notice the following things. First, $\alpha(v_d)$ approaches -2 rather than -3. Figure 8(d) denies the approach to -3 for all the values of h computed, and Fig. 8(c) supports that $\alpha(v_d) \to -2$, at least in the case of $h = 1 \times 10^{-1}$, 5×10^{-2}, and 2.5×10^{-2}. However, Fig. 8(c) tells that the rate of approach of $\alpha(v_d) \to -2$ is slower for $h < \infty$. In summary, the rate of approach may be described by

$$|v_{B\infty} - v_B(t)| \approx C_h t^{-2} \quad \text{for} \quad t \gg 1, \tag{38}$$

where $C_h > 0$ is a positive constant. It is seen from Fig. 8 that C_h is an increasing function of h, and the limiting values are $C_h \to C_0$ for $h \to 0$ and $C_h \to C_\infty$ for $h \to \infty$. For a finite h, the faster power law t^{-3} would hold transiently, and the slower power law t^{-2} would appear for sufficiently large t.

The results for different $v_{B\infty} = 0.5$, shown in Fig. 9, exhibit the qualitatively similar behaviors of v_d and its gradient. Hence, the above-mentioned behavior of v_d is not a particular one for a specific $v_{B\infty}$.

C. Error estimate

In this section, we estimate the error contained in the present numerical analysis using the case of $v_{B\infty} = 2$ and $h = 0.1$ with different numerical parameters. As a reference case (Case 1), we choose the parameter set (37). The different numerical parameters are used in the following cases:

$$\text{Case 2a: } N_{x_2} = 8, \quad \text{Case 2b: } N_{x_2} = 16, \tag{39a}$$

$$\text{Case 3a: } N_{2\,\rm min} = 8, \quad \text{Case 3b: } N_{2\,\rm min} = 16, \tag{39b}$$

$$\text{Case 4a: } N_{1\,\rm min} = 20, \quad \text{Case 4b: } N_{1\,\rm min} = 40, \tag{39c}$$

$$\text{Case 5a: } \Delta t = 0.025, \quad \text{Case 5b: } \Delta t = 0.0125. \tag{39d}$$

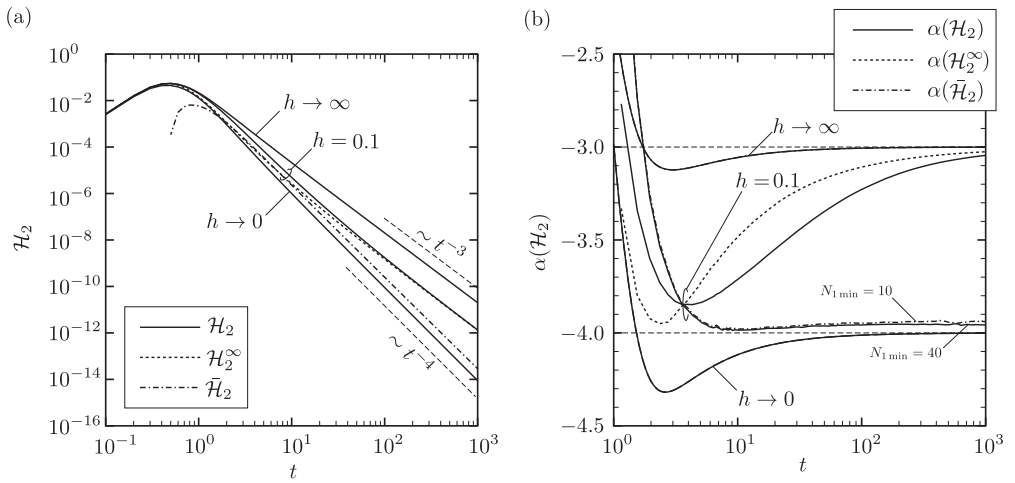

FIG. 7. (a) Profiles of the history term $\mathcal{H}_2$ (solid), $\mathcal{H}_2^\infty$ (dashed), and $\bar{\mathcal{H}}_2$ (dash-dot) [cf. Eq. (30a)] versus t in the double logarithmic scale for cases $h \to \infty$, $h = 0.1$, and $h \to 0$. (b) The gradients of curves in panel (a) [cf. Eq. (36)]. For $\alpha(\bar{\mathcal{H}}_2)$, two curves are presented: the one obtained with $N_{1\,\mathrm{min}} = 10$ (dash-dot) and the one obtained with $N_{1\,\mathrm{min}} = 40$ (solid).

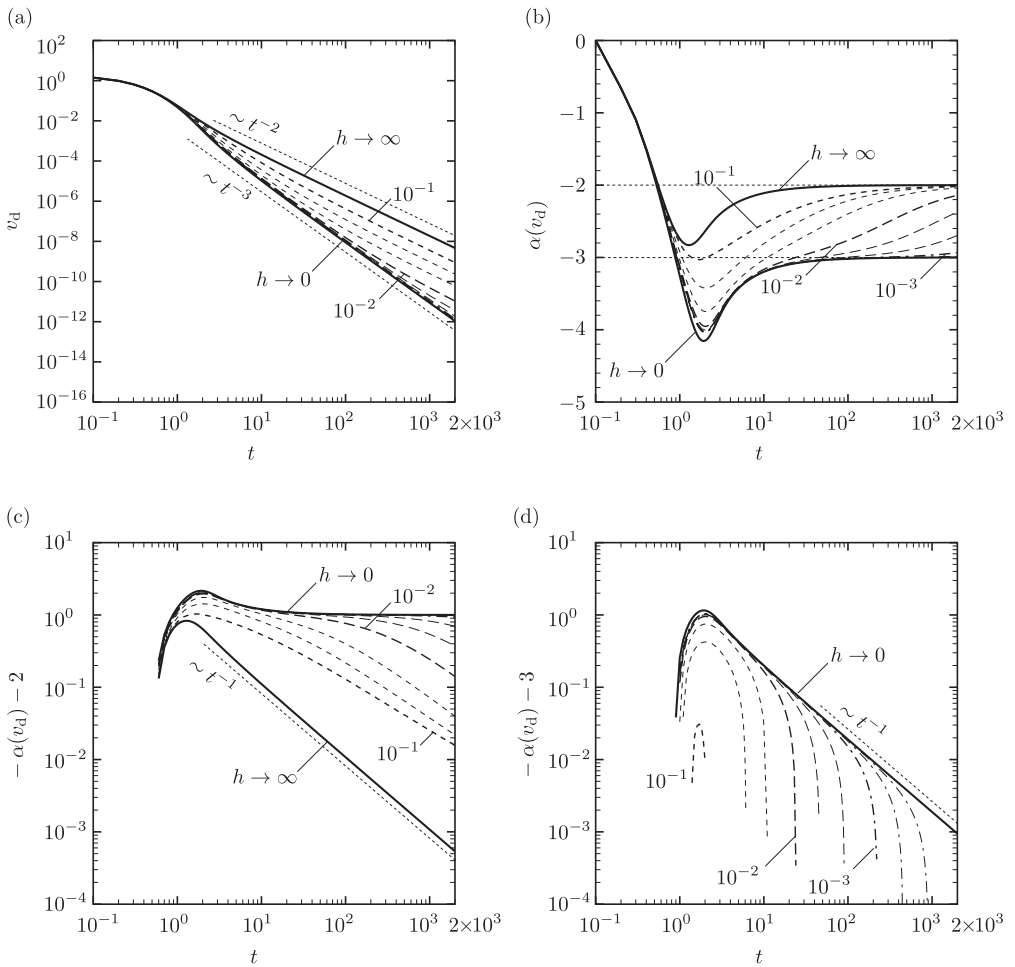

FIG. 8. The long-time behavior of v_d [cf. (35)] and $\alpha(v_d)$ in the case of $v_{B\infty} = 2$. The results with $h \to \infty$ and $h \to 0$ are shown with a bold solid line; those with $h = 1 \times 10^{-1}$, 5×10^{-2}, and 2.5×10^{-2} are shown by a dashed line; those with $h = 1 \times 10^{-2}$, 5×10^{-3}, 2.5×10^{-3} are shown by a long-dashed line; those with $h = 1 \times 10^{-3}$, 5×10^{-4}, 2.5×10^{-4} are shown by a dash-dot line. The curves for $h = 10^{-1}$, 10^{-2}, and 10^{-3} are slightly thickened. (a) v_d, (b) $\alpha(v_d)$, (c) $-\alpha(v_d) - 2$, and (d) $-\alpha(v_d) - 3$.

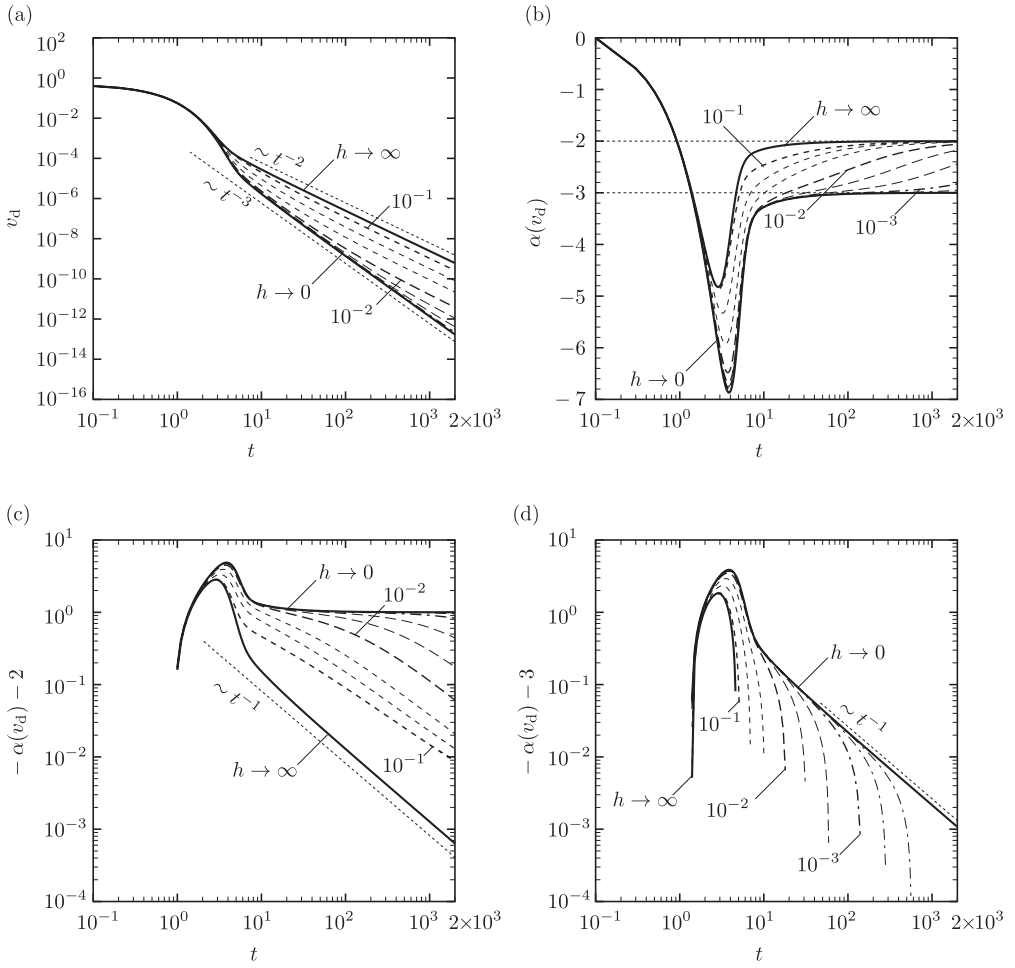

FIG. 9. The long-time behavior of v_d [cf. (35)] and $\alpha(v_d)$ in the case of $v_{B\infty} = 0.5$. See the caption to Fig. 8.

The values of v_d and $-\alpha(v_d) - 2$ for times $t = 1, 10, 10^2$, and 10^3 are shown in Tables I and II, respectively. It is seen from both tables that the errors in all cases are sufficiently small to support the discussion in Secs. V A and V B. To see the tables in detail, we define the relative change by the absolute difference between the results of Case 1 and Case X (X = 2a, 2b, ..., 5b) divided by the result of Case 1. The relative changes of Cases 2, Case 3, Case 4, and Case 5 for v_d are less than 10^{-3}%, 10^{-3}%, 0.05%, and 0.5%, respectively, for $t = 10^3$. The relative changes of Cases 2, Case 3, Case 4, and Case 5 for $\alpha(v_d)$ are less than 0.1%, 0.01%, 5%, and 0.5%, respectively, for $t = 10^3$. The comparatively large error in Case 3 is due to the presence of the sharp point caused by the nonuniform decay of $\bar{Q}_2$ presented in Fig. 6. We have checked that the

TABLE I. The values of v_d for Case 1, Case 2a, Case 2b, ..., Case 5b. The parameters are set to $v_{B\infty} = 2$ and $h = 0.1$.

	v_d				
t	Case 1	Case 2a	Case 2b	Case 3a	Case 3b
1(0)	5.61708(−2)[a]	5.61640(−2)	5.61623(−2)	5.61709(−2)	5.61714(−2)
1(1)	8.18155(−5)	8.17898(−5)	8.17825(−5)	8.18173(−5)	8.18183(−5)
1(2)	4.14948(−7)	4.14914(−7)	4.14903(−7)	4.14950(−7)	4.14952(−7)
1(3)	3.58237(−9)	3.58223(−9)	3.58219(−9)	3.58238(−9)	3.58239(−9)
t	–	Case 4a	Case 4b	Case 5a	Case 5b
1(0)	–	5.62591(−2)	5.62762(−2)	5.62919(−2)	5.63334(−2)
1(1)	–	8.08189(−5)	8.05976(−5)	8.14404(−5)	8.13938(−5)
1(2)	–	4.13266(−7)	4.12869(−7)	4.13948(−7)	4.13812(−7)
1(3)	–	3.58144(−9)	3.58119(−9)	3.57605(−9)	3.57509(−9)

[a]Read as 5.61708×10^{-2}.

TABLE II. The values of $-\alpha(v_d)-2$ for Case 1, Case 2a, Case 2b, ..., Case 5b. The parameters are set to $v_{B\infty}=2$ and $h=0.1$.

	$-\alpha(v_d)-2$				
t	Case 1	Case 2a	Case 2b	Case 3a	Case 3b
1(0)	8.04486(−1)[a]	8.04927(−1)	8.05031(−1)	8.04480(−1)	8.04435(−1)
1(1)	5.34833(−1)	5.34416(−1)	5.34463(−1)	5.34858(−1)	5.34866(−1)
1(2)	1.28943(−1)	1.28881(−1)	1.28858(−1)	1.28949(−1)	1.28951(−1)
1(3)	2.53877(−2)	2.53725(−2)	2.53678(−2)	2.53887(−2)	2.53893(−2)
t	–	Case 4a	Case 4b	Case 5a	Case 5b
1(0)	–	8.01678(−1)	8.02973(−1)	8.23683(−1)	8.30970(−1)
1(1)	–	5.32306(−1)	5.32059(−1)	5.33293(−1)	5.33199(−1)
1(2)	–	1.26029(−1)	1.25251(−1)	1.28304(−1)	1.28279(−1)
1(3)	–	2.46562(−2)	2.44486(−2)	2.53090(−2)	2.53341(−2)

[a]Read as 8.04486×10^{-1}.

value of $Z=5$ is sufficient and the computation with larger Z results in negligibly small difference compared with the differences discussed in Tables I and II.

VI. CONCLUSION

The motion of a concave body in a free-molecular gas under a constant external force is studied numerically, with special interest on the rate of approach to the terminal velocity $v_{B\infty}$. The boundary condition on the base plate is diffuse reflection and that on the lateral plates are specular reflection. Since the lateral plates do not give rise to an additional drag force but only play a role of preventing the molecule from escaping to infinity, the present setting can elucidate solely the effect of the concavity arising from the lateral plates. It is found that the rate of approach can be described as $|v_{B\infty}-v_B|\approx C_h t^{-2}$ for $h>0$, which is slower than the rate $|v_{B\infty}-v_B|\approx C_0 t^{-3}$ found in the previous study [18] for $h=0$. The slower approach for $h>0$ is due to the molecules trapped by the concavity. We have visualized the effect of trapped molecules at the level of the velocity distribution function and its moments. As a result, the velocity distribution function is shown to be a piecewise continuous function in (ζ_1,ζ_2) space and has the complex shape. The numerical method used in the present paper captures the exact shape of the complex velocity distribution function and correctly describes the time development of the moments (i.e., nonuniformity with respect to $\zeta_1^{\rm nor}$).

As the continuation of previous works [10–14,16–22] (see also the monograph [23]) that aim to clarify the microscopic dynamics of the friction acting on a moving obstacle, the present study together with Ref. [15] clarify that a simple concavity of a body may affect the time-dependent motion qualitatively. Note that the shape of the body in the present study may be the special class of concave bodies. Therefore, it is not surprising if a qualitatively different behavior is observed for different (more general) concavities. However, as expected from the description in Secs. III and V A, a slight change of the body shape may result in the drastic change of the computation as well as the shape of the velocity distribution function. Therefore, we have restricted ourselves to the detailed investigation of the simplest case with great accuracy in the present paper. The effect of different concavities, intermolecular collisions (cf. Refs. [21,22]), initial velocities larger than the terminal velocity (cf. Ref. [11]), and different boundary conditions (cf. Refs. [16,17]) are the subject of future works.

APPENDIX A: ALGORITHM TO OBTAIN $\bar{\Gamma}_2$

As in the main text, we consider only a positive ζ_2. Suppose that a recolliding molecule hits the lateral plates $\tilde{n}$ times. Then, at least, the velocity ζ_2 must satisfy the following:

$$\zeta_2\in[z_{\tilde{n}},z_{\tilde{n}+1}],\quad z_{\tilde{n}}=\frac{x_2+(2\tilde{n}-1)/2}{t-t^b}. \tag{A1}$$

For such a molecule, the condition $\{t_k\in[t^b,\tau_-]\cup[\tau_+,t],\ {}^\forall k=1,\dots,\tilde{n}\}$ [cf. $\bar{\Gamma}_2$ in Eq. (24)] can be rewritten as

$$\{\zeta_2\in[z_k,\gamma_- z_k]\cup[\gamma_+ z_k,\infty),\ {}^\forall k=1,\dots,\tilde{n}\}, \tag{A2}$$

where $\gamma_\pm=(t-t^b)/(t-\tau_\pm)$, $(1<\gamma_-<\gamma_+<\infty)$. Therefore, the velocity ζ_2 of the recolliding molecule, which makes $\tilde{n}$ times reflections by the lateral plates, is included in the intersection of Eqs. (A1) and (A2). Then, $\bar{\Gamma}_2$ can be expressed as the sum of such intersections for all $\tilde{n}=0,\dots,\infty$. Note that for $\tilde{n}=0$ we only use Eq. (A1), and thus we mention $\tilde{n}=1,\dots$ in the following.

Let us introduce $a_k=\gamma_- z_k$ and $b_k=\gamma_+ z_k$ (cf. $a_k<b_k$, $a_k<a_{k+1}$, $b_k<b_{k+1}$). In addition, we introduce a subset of $\mathbb{R}$ as $\Omega_1=[z_1,a_1]\cup[b_1,\infty)$. We call a semi-infinite segment $[b_1,\infty)$ a last segment (Fig. 10). Then we transform Ω_1 to Ω_2 under the following rule (see also Fig. 10 for the visualization of the rule):

(a) If $a_2<b_1$, the lower end of the last segment is replaced by b_2. That is, $\Omega_1\to\Omega_2=[z_1,a_1]\cup[b_2,\infty)$.

(b) If $a_2\geqslant b_1$, the upper end of the last segment is replaced by a_2. Moreover, a new segment is added after the last segment, and the new segment becomes a new last segment. The lower and upper ends of the new last segment are, respectively, b_2 and ∞. That is, $\Omega_1\to\Omega_2=[z_1,a_1]\cup[b_1,a_2]\cup[b_2,\infty)$.

By iterating the above procedure until the necessary region of ζ_2 space is covered, we finally obtain $\bar{\Gamma}_2$ as Ω_k, which consists of several segments on which the velocity distribution function $g_{B+}-E$ (i.e., the contribution of recollision) is nonzero [cf. Eq. (15)].

Note that there always exists an integer k' such that $a_{k+1}<b_k$ $({}^\forall k>k')$. If we iterate the above transformation

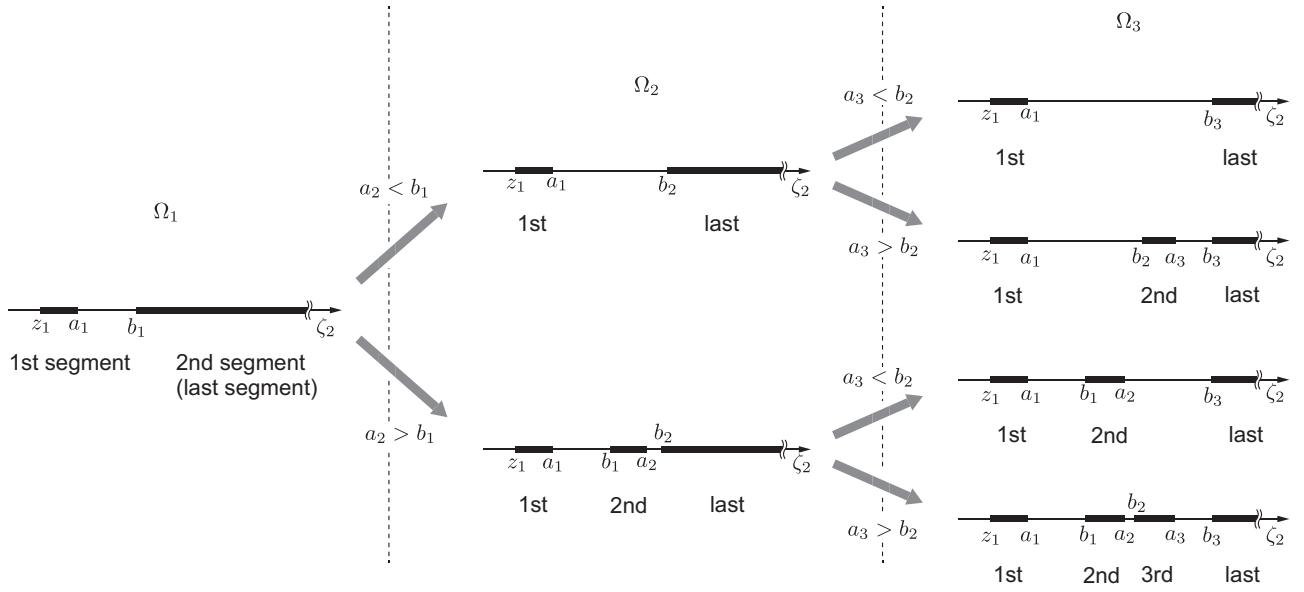

FIG. 10. Schematic diagram of Ω_1, Ω_2, and Ω_3, which are represented by bold segments. Depending on the relation between a_{k+1} and b_k, the number and the range of segments, i.e., the support of $g_{B+} - E$ [cf. Eq. (15)], vary.

of Ω_k infinitely many times, the lower end of the last segment goes to infinity. Therefore, $\zeta_2 \to \infty$ is not included in $\bar{\Gamma}_2$, namely the last segment is not included in $\bar{\Gamma}_2$.

APPENDIX B: ALGORITHM TO OBTAIN t^b, τ, AND $\tau_\pm$

In the numerical analysis, the trajectory of the base plate $x_B(t)$ is expressed as the connection of m segments $\ell_B^{(m')}$ ($m' = 0, \ldots, m-1$):

$$\ell_B^{(m')} : \; x_1 = \frac{t - t^{(m')}}{\Delta t} x_B^{(m'+1)} - \frac{t - t^{(m'+1)}}{\Delta t} x_B^{(m')} \quad \text{for} \quad t \in [t^{(m')}, t^{(m'+1)}]. \tag{B1}$$

Here t is a dummy variable that runs from 0 to $t^{(m)}$. The molecular path of a molecule that hits the base plate at time $t^{(m)}$ is expressed as

$$\ell_M : \; x_1 = x_B^{(m)} - \zeta_1 [t^{(m)} - t]. \tag{B2}$$

Since we treat only the case where the velocity of the body is monotonically increasing, the connection of segments $\ell_B^{(m')}$ and the molecular path ℓ_M with $\zeta_1 \in \Gamma_1$ has only one intersection in (x_1, t) space. The time at the intersection is obtained as t^b [cf. Fig. 3(a)].

Next we introduce the trajectory of the tip $x_B(t) + h$ as

$$\ell_T^{(m')} : \; x_1 = \frac{t - t^{(m')}}{\Delta t} x_B^{(m'+1)} - \frac{t - t^{(m'+1)}}{\Delta t} x_B^{(m')} + h \quad \text{for} \quad t \in [t^{(m')}, t^{(m'+1)}]. \tag{B3}$$

The connected segments $\ell_T^{(m')}$ and the molecular path ℓ_M with $\zeta_1 \in \bar{\Gamma}_1$ have two intersections in (x_1, t) space. We define these times corresponding to those two intersections as τ_- and $\tau_+ (> \tau_-)$ [cf. Fig. 3(c)].

Finally, the tangential line in Fig. 3(c) and the contact point is obtained as follows. Since we consider the discrete trajectory (B3), the tangential line from a point (x_B, t) to Eq. (B3) has the slope between the slopes of two segments that share the contact point. In other words, letting $[x_B^{(m_\sharp)}, t^{(m_\sharp)}]$ be the contact point, it satisfies the following relation:

$$\begin{aligned} \tau &= t^{(m_\sharp)}, \\ m_\sharp &= \{ {}^\exists m' = 1, \ldots, m-1 | [s^{(m')} - \zeta_{1\sharp}^{(m')}] \\ &\qquad \times [s^{(m'+1)} - \zeta_{1\sharp}^{(m')}] < 0 \}, \end{aligned} \tag{B4a}$$

$$\begin{aligned} s^{(m')} &= \frac{x_B^{(m')} - x_B^{(m'-1)}}{\Delta t}, \\ \zeta_{1\sharp}^{(m')} &= \frac{x_B^{(m)} - \left[x_B^{(m')} + h \right]}{t^{(m)} - t^{(m')}}. \end{aligned} \tag{B4b}$$

A velocity $\check{v}_{B,\tau}$ in the main text is then given by $\check{v}_{B,\tau} = \zeta_{1\sharp}^{(m')}$.

[1] A. B. Basset, *A Treatise on Hydrodynamics: With Numerous Examples*, Vol. 2 (Deighton, Bell and Company, Cambridge, 1888).

[2] R. Clift, J. R. Grace, and M. E. Weber, *Bubbles, Drops, and Particles* (Academic Press, New York, 1978).

[3] M. R. Maxey and J. J. Riley, Phys. Fluids **26**, 883 (1983).

[4] A. Belmonte, J. T. Jacobsen, and A. Jayaraman, Electron. J. Differ. Eq. **2001**, 1 (2001).

[5] C. J. Lawrence and R. Mei, J. Fluid Mech. **283**, 307 (1995).

[6] A. Daitche and T. Tél, Phys. Rev. Lett. **107**, 244501 (2011).

[7] N. Mordant and J.-F. Pinton, Eur. Phys. J. B **18**, 343 (2000).

[8] C. Cercignani, R. Illner, and M. Pulvirenti, *The Mathematical Theory of Dilute Gases* (Springer, Berlin, 1994).
[9] Y. Sone, *Molecular Gas Dynamics: Theory, Techniques, and Applications* (Birkhauser, Boston, 2007).
[10] S. Caprino, C. Marchioro, and M. Pulvirenti, Commun. Math. Phys. **264**, 167 (2006).
[11] S. Caprino, G. Cavallaro, and C. Marchioro, Math. Model. Method. Appl. Sci. **17**, 1369 (2007).
[12] G. Cavallaro, Rend. Mat. Appl **27**, 123 (2007).
[13] K. Aoki, G. Cavallaro, C. Marchioro, and M. Pulvirenti, ESIAM Math. Modell. Numer. Anal. **42**, 263 (2008).
[14] G. Cavallaro and C. Marchioro, Rep. Math. Phys. **69**, 251 (2012).
[15] F. Sisti and C. Ricciuti, SIAM J. Math. Anal. **46**, 3579 (2014).
[16] X. Chen and W. Strauss, Arch. Ration. Mech. Anal. **211**, 879 (2014).
[17] X. Chen and W. Strauss, Commun. Math. Phys. **338**, 139 (2015).
[18] K. Aoki, T. Tsuji, and G. Cavallaro, Phys. Rev. E **80**, 016309 (2009).
[19] T. Tsuji and K. Aoki, in *27th International Symposium on Rarefied Gas Dynamics*, Vol. 1333 (American Institute of Physics, Melville, 2011), p. 140.
[20] T. Tsuji and K. Aoki, J. Stat. Phys. **146**, 620 (2012).
[21] T. Tsuji and K. Aoki, J. Comput. Phys. **250**, 574 (2013).
[22] T. Tsuji and K. Aoki, Phys. Rev. E **89**, 052129 (2014).
[23] P. Buttà, G. Cavallaro, and C. Marchioro, in *Mathematical Models of Viscous Friction* (Springer, Berlin, 2015), pp. 63–100.
[24] J. Fröhlich, Z. Gang, and A. Soffer, Commun. Math. Phys. **315**, 401 (2012).
[25] P. Buttà, E. Caglioti, and C. Marchioro, Commun. Math. Phys. **233**, 545 (2003).